COMMUNICATION

Biologically Inspired, Sophisticated Motions from Helically Assembled, Conducting Fibers

Peining Chen, Yifan Xu, Sisi He, Xuemei Sun, Wenhan Guo, Zhitao Zhang, Longbin Qiu, Jianfeng Li, Daoyong Chen, and Huisheng Peng**

Biological motions, such as the wing flapping of flying creatures and the body undulation of reptiles, are produced to perform sophisticated functions through the synergetic interactions of muscles and nerve systems.[1–4] To mimic these motions in robots, complex mechanical components are required; however, their miniaturisation is a challenge governed by force-scaling laws, and unconventional solutions are needed for propulsion, actuation, and manufacturing.[5–7] Thus, designing and fabricating high-power-density artificial muscles using a convenient and efficient method is important.[8–10]

Carbon nanotubes have been extensively explored as a functional material due to their unique one-dimensional structure and remarkable properties including their light weight, high tensile strength, high electrical conductivity, and large surface area.[11–15] Unexpectedly, helically and hierarchically assembled macroscopic multi-walled carbon nanotube (MWCNT) fibers[16–18] have been found to simultaneously display a contractive and torsional actuation upon the application of low electric currents, and tunable motions are created from the three-dimensional electromechanical actuation of single fibers without complex architectures. Because of the high tensile strength on the level of 10^3 MPa and electrical conductivity on the order of 10^3 S/cm in the MWCNT fiber, the actuation may generate a stress more than 260 times the typical natural skeletal muscle with high reversibility,[19] good stability, high work density, extremely low functioning electric field, and availability to various media.

The formation of MWCNT fibers is schematically shown in **Figure 1**a. A helical primary MWCNT fiber is first continuously dry-spun from an MWCNT array synthesised by chemical vapour deposition (Figure S1 and Movie S1). Both the left and right-handed MWCNT fibers can be produced by changing the twisting direction during spinning. Figure 1b shows the scanning electron microscopy (SEM) image of a left-handed fiber with a helical angle of approximately 32° and a uniform diameter of 16 μm. The used MWCNT had an average diameter of approximately 10 nm, and the number density of the MWCNTs was calculated as approximately 6×10^{11} cm^{-2}. The MWCNTs were highly aligned along the helical direction (Figure 1c). The prepared fibers were further twisted to form the desired secondary fiber by stabilising one end while rotating the other end (Figure S2). A series of secondary fibers with increasing helical angles were formed by varying the rotary speed and time, and the left-handed helical structure was primarily used in the following study unless specified. Figures 1d-i show the secondary fibers with increasing helical angles of approximately 6°, 19°, 24°, 31°, 37°, and 43°, respectively, based on the same primary fiber. These secondary fibers varied from 110 to 140 μm in diameter, and the primary fibers were also aligned in a format similar to the MWCNTs in the primary fiber (Figures 1j and S3). The secondary fibers were flexible and strong and could be further shaped into various forms, such as a spring (Figure 1k), using thermo-hydro treatments.

A single secondary fiber was attached to a paper in a curved structure, which then produced a unique motion similar to that of a wing (**Figure 2**a). The paper flapped up upon applying a current and returned to its original position after the current was disconnected (Movie S2). Figure 2b further shows the motion trail over a period of 1 s with the current passed at 0 ms and disconnected at 500 ms. The flapping angle was sharply increased at 66.7 ms and slightly increased until 266.7 ms. Upon removal of the current, the artificial wing rapidly returned to the original state. The motion trail was further quantitatively analysed using a frame-by-frame method (Figures 2c and d). The maximal flapping angle was approximately 43° at 50 mA with 19.1° completed in the first 33.3 ms. The initial average angular velocity reached 570°/s; however, the weight of the artificial wing was 100 times larger than that of the secondary fiber. The flapping frequency was the same as the current frequency at below 1 Hz and slightly lagged at higher frequencies because of the relatively higher load of the attached paper (Figure 2d). The flapping frequency could be tuned by varying the frequency of the passed current; the flapping frequency was comparable with that of a butterfly.

A single secondary fiber can be folded and twisted into a larger helical fiber similar to the supercoiled structure of DNA at a middle point (Figures 1l-n). When a glass bar (with a weight of 5000 times the fiber) was fixed at the folding point (Figure S4), the bar rotated when a current was applied. The maximum rotary angle reached approximately 180° (Figure S5 and Movie S3). After removal of the glass bar, a tunable and complex motion similar to a wagging animal tail was produced (**Figure 3**a). When a pulse current with a magnitude of

P. Chen, Y. Xu, S. He, Dr. X. Sun, W. Guo, Z. Zhang, L. Qiu, Dr. J. Li, Prof. Dr. D. Chen, Prof. Dr. H. Peng
State Key Laboratory of Molecular Engineering of Polymers
Department of Macromolecular Science and Laboratory of Advanced Materials
Fudan University
Shanghai 200438, China
E-mail: lijf@fudan.edu.cn; penghs@fudan.edu.cn

DOI: 10.1002/adma.201402867

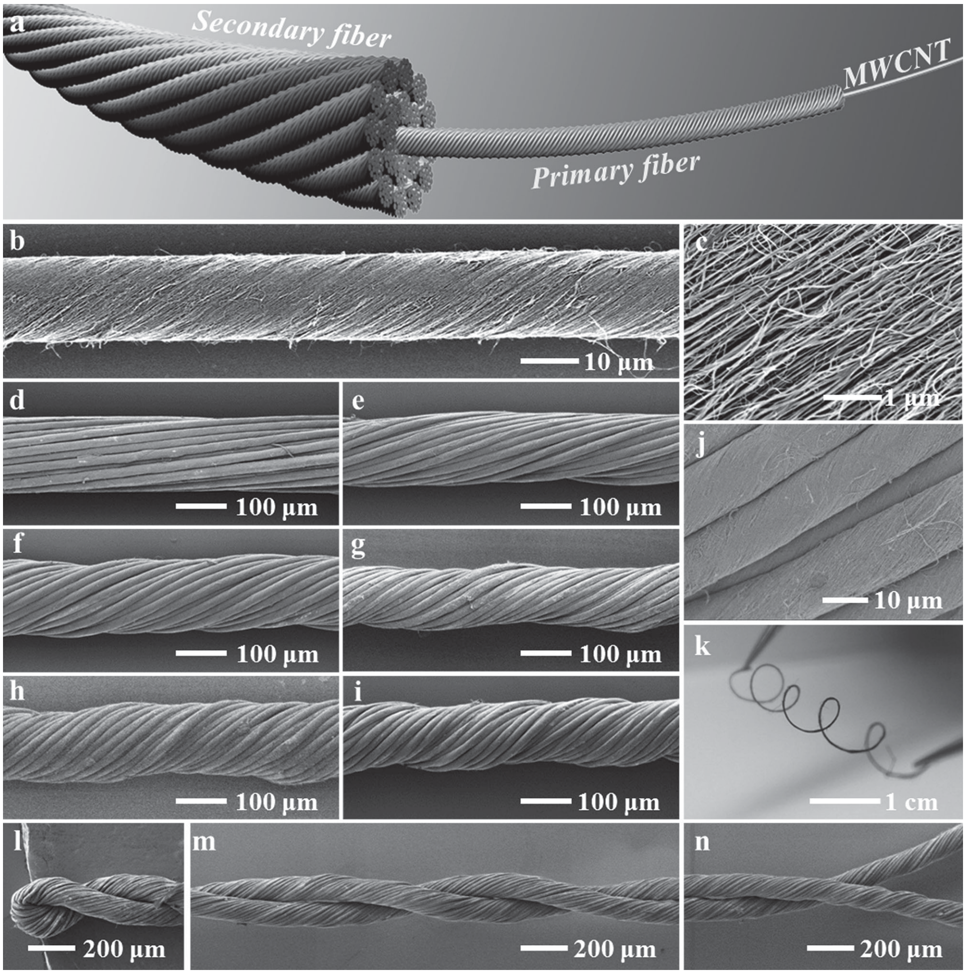

Figure 1. SEM images of hierarchically and helically assembled MWCNT fibers at three levels. a) Schematic illustration of the helical assembly of MWCNTs into primary and secondary fibers. b) A primary fiber assembled from aligned MWCNTs with a helical angle of approximately 32°. c) Higher magnification of (g). d-i) Secondary fibers assembled from 50 primary fibers with increasing twisting angles of appropriately 6°, 19°, 24°, 31°, 37° and 43°, respectively. j) Higher magnification of (f). k) Photograph of a secondary fiber being shaped into a spring structure after a thermo-hydro treatment. l-m) A secondary fiber being bent and twisted.

125 mA was passed through the fiber at 0 ms and disconnected at 500 ms over a period of 1 s, because the tail section marked by a red dot was not fixed, it could move flexibly during the actuation process (Movie S4). Both the speed of motion and amplitude were high for the first 233 ms and then reduced for the following 267 ms. After removing the current, the tail rapidly swung back to its original state.

To better understand the motion of the tail end, it was traced by high-speed cameras upon the addition of both pulse and linear currents (Movies S5 and S6) and reconstructed through a frame-by-frame analysis (Figure 3b). The end of the tail could reverse back to the original point along the forwarding path after removal of the current, and the reversible motions could be repeated with high stability (Figures 3c and S6). Note that the "power off" curve was more fluctuated than the "power on" curve in Figure 3c. This phenomenon may be explained by the fact that the fiber movement under the electromechanical actuation was fast, while the recovery motion of the fiber was much slower. Therefore, the recovery motion would be more affected by the atmosphere with larger fluctuations, particularly considering that the MWCNT fiber was flexible and lightweight. To quantitatively describe the trajectory, a one-dimensional motion trajectory along the Z axis was further extracted (Figure 3d). The tail end swung to its highest point within less than 0.1 s upon passing the current and reversed back to its original point by 0.5 s. The linear swinging velocity reached ~1.75 m/s in 7.5 ms with an initial accelerated velocity of ~90 m/s^2 (Figure 3e), which was greater than 10 times that of a cheetah.[20] Although the three-dimensional trajectory for the linear current was similar to that for the pulse current (Figure S7), the real-time swinging trajectory was different (Figure 3f); for example, the swing amplitude was slightly increased within the initial 0.4 s and then largely increased when a linear electric current with a scan rate of 117 mA/s was passed through the tail. In addition, the tail end could be accurately controlled by varying the current magnitude with good durability. For example, the tail end was maintained at 2.1, 3.2 and 4.0 mm along the Z-axis for more than half an hour at 60, 80 and 120 mA, respectively (Figure 3g).

The trajectory of the tail end was similar to an arc and can be described by the motion of the angle (Figures S8 and S9)

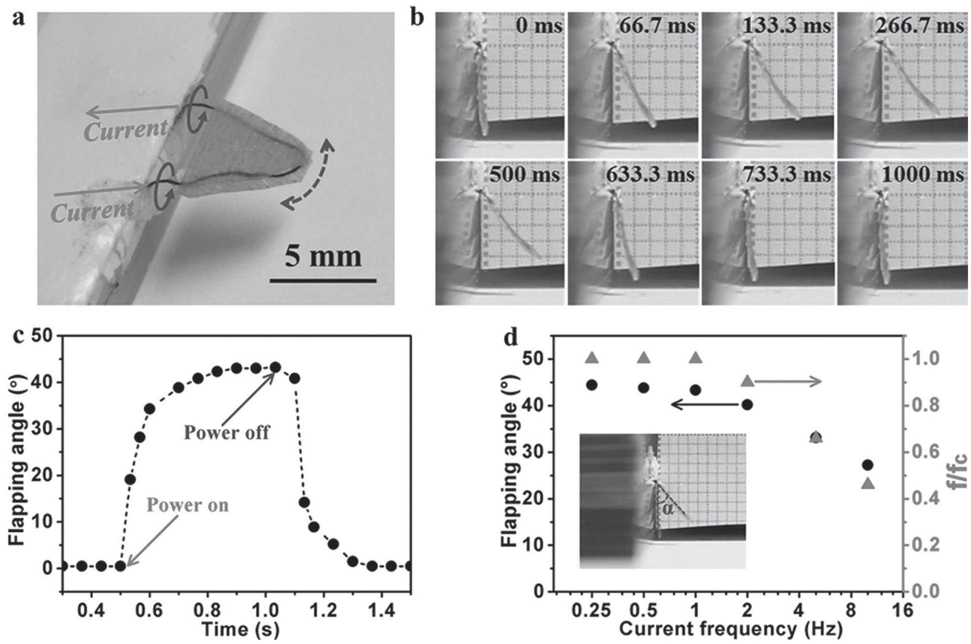

Figure 2. Flapping motion of artificial wing. a) Schematic illustration of an artificial wing. b) Photographs of the motion trail when the artificial wing was flapped up and down upon the addition of a current of 50 mA over a period of 1 s. The current was turned on at t_0 (0 s) and off at t_4 (500 ms). c) Dependence of the flapping angle on time. d) Dependence of the flapping angle and ratio of f/f_c on the current frequency. Here, f_c and f correspond to the current frequency and measured flapping frequency of the artificial wing, respectively.

using an exponential decay equation: $\theta(t) = \theta_{eq} + \Delta\theta e^{-t/\tau}$. The motion equation can be obtained as follows (see Supporting Information):

$$\frac{d\theta(t)}{dt} = -\alpha t^2[\theta(t) - \theta_{eq}] \tag{1}$$

Herein, $\theta(t) = \theta_{eq} + \Delta\theta \exp(-\alpha t^3/3)$, where R = 4.99 cm, θ_{eq} = 3.96, $\Delta\theta = 1.26$ and $\alpha = 8.1855\ s^{-3}$ at a current-increasing rate of 117 $mA \cdot s^{-1}$. Clearly, the fitted curve matches the experimental data well (Figure S10), verifying that the quadratic power law obtained by the scaling analysis was reasonable.

The sophisticated and controlled motions were produced by a contractive and torsional electromechanical actuation. To understand the unique actuation of the secondary fibers, the primary fiber was investigated (Figures S11-14). For the primary MWCNT fiber, the maximal contractive stress occurred at a helical angle of 32° that was used to prepare the secondary fiber if not specified (Figure S12). The secondary fiber rotated in opposite directions at the two ends when the middle part remained motionless (Movie S7). The generated contractive stress was dependent on the helical angle of the secondary fiber, and a maximal value of over 21 MPa occurred at a helical angle of appropriately 31° (**Figure 4**a). In addition, the contractive stress was increased with the increasing current at the investigated range under the same other conditions such as a helical angle of 31° (Figure 4b). The contractive stress reached 26.3 MPa at 150 mA, more than 260 times of natural skeletal muscles. As expected, the rotary angle was also increased with the increasing current (Figure 4b). The rotary angle was continuously increased as the current increased, and a rotary angle of approximately 65° was obtained at 150 mA (Figure 4b and Movie S8), which was appropriately twice that of the primary fiber with a helical angle of 32° even though the used power density in the secondary fiber was only one-seventh of the power density in the primary fiber (Figure S14). The electromechanical actuation was fast and could be completed in milliseconds (Figure 4c). In addition, the maximal rate of the stress output reached 230 MPa/s. The secondary fiber showed high electromechanical reversibility, and no obvious decrease was found in the contractive stress after 1000 cycles (Figure S15).

The contractive actuations were carefully compared for the non-helical primary fibers, helical primary fibers, and the corresponding secondary fibers under similar power densities (Figure 4d). The primary fiber with a helical angle of 32° generated a stress of 2 MPa compared with 0.85 MPa of its non-helical counterpart. The produced stress from a non-helical fiber was derived from the fact that MWCNTs are not perfectly aligned along the axial direction. Interestingly, the generated stress was magnified from the primary to secondary fibers. For example, the contractive stresses of the helical secondary fibers that were composed of 50 helical primary fibers (helical angle of approximately 32°) increased to 3.3, 6.6, 11.9 and 19.1 MPa as the secondary helical angle increased to 6°, 19°, 24° and 31°, respectively. The highest stress of 19.1 MPa (A_4 in Figure 4d) was more than 9 times larger than that of its component primary fiber (A_0 in Figure 4d). A similar dependence of the contractive stress on the helical angle was also discovered for the secondary fibers prepared from non-helical primary fibers (Figure S16). The maximum contractive stress at a secondary helical angle of approximately 35° was 11.8 MPa (B_4 in Figure 4d), which was more than 14 times that of its component non-helical primary fiber (B_0 in Figure 4d). In addition, the contractive stress produced by the secondary fiber assembled from

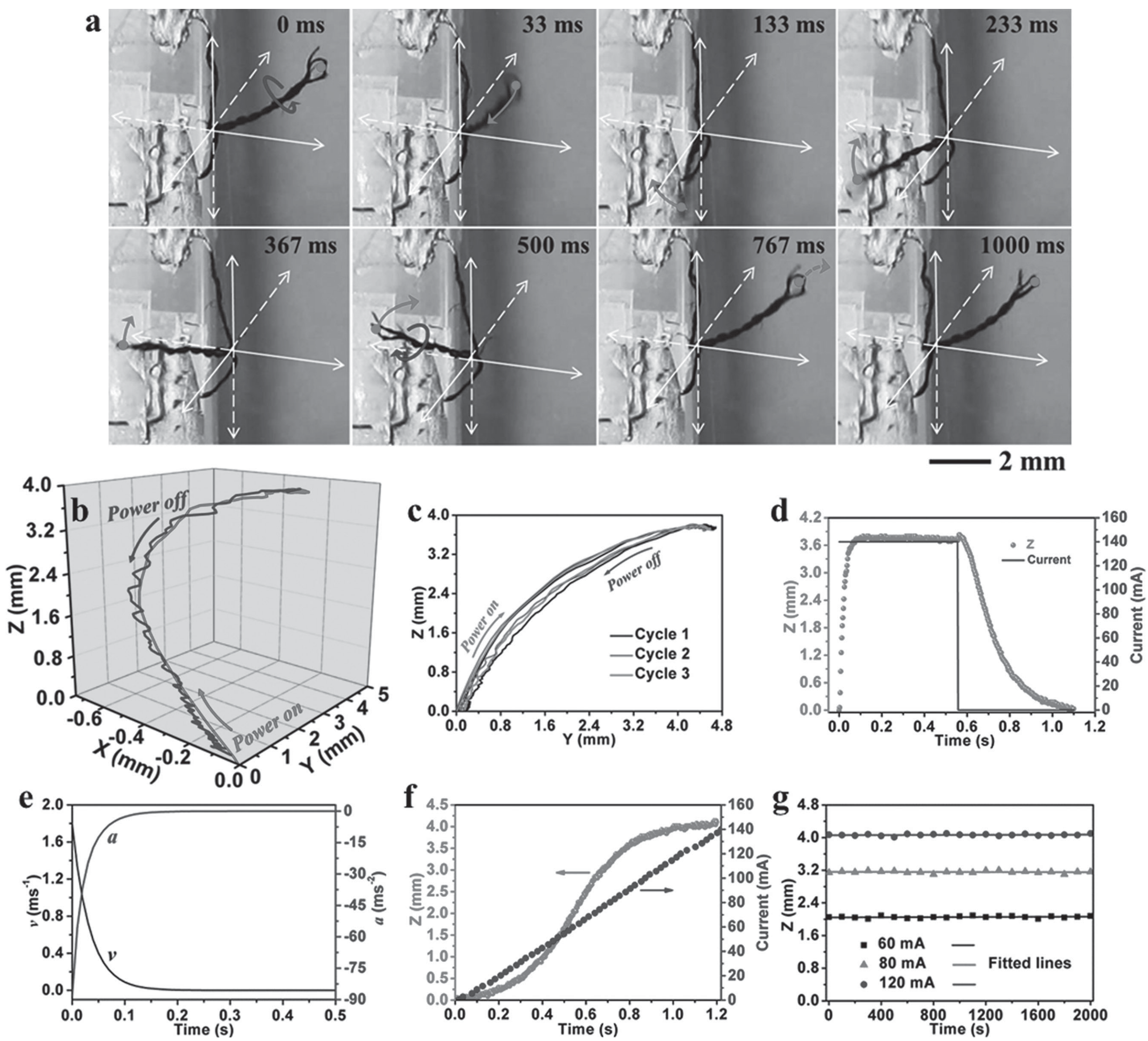

Figure 3. Waggling motion of an artificial tail. a) Photographs of the motion trail of a self-twisted secondary fiber with two fixed ends. The used secondary fiber was assembled from 50 primary fibers (helical angle of 35°) with a secondary helical angle of approximately 31°. A current of 125 mA was passed through the fiber, and a period of 1 s was studied with the current turned on and off at 0 and 500 ms, respectively. b) Three-dimensional trajectories upon the addition of a pulse current of 140 mA. c) Projective trajectories on the Y-Z plane for three cycles by passing a pulse current of 140 mA. d) Dependence of the displacement along the Z-axis on time. e) Dependence of the linear velocity and accelerated velocity on time. f) Dependence of the displacement along the Z-axis on time upon the addition of a linear current with a scan rate of 117 mA/s. g) Displacement of the tail end along the Z-axis upon the addition of a current (60, 80 and 120 mA) for 2000 s.

the helical primary fibers was much higher than that from the non-helical primary fibers, i.e., 1.5-2 times at similar secondary helical angles of 30-37°.

The thermal expansion coefficient for the fiber was calculated to be at the level of -10^{-6}/°C; thus, the contribution of the Joule heat to the contractive stress is negligible.[21–23] Here, a scaling analysis (see Supporting Information) showed that the contractive and rotary actuations could be explained by Ampere's Law and the Law of the Lever, in which the mechanical property of the fiber also plays an important role (Figures 4e-g). The electromagnetic force governed by Ampere's Law was the primary driving force for the actuation but was too weak, whereas the Law of the Lever could amplify the force to an observable scale. The amplification magnitude depended on the stiffness of the primary or secondary fibers by considering individual MWCNTs or primary fibers as levers. For a better understanding of the electromechanical actuations generated by the primary and secondary fibers, a detailed simulation and analysis is provided in the Supporting Information. It shows that the simulated results (Figure S17) agreed well with the experimental observations, verifying that the mechanism on basis of Ampere's Law and the Law of the Lever was reasonable.

Note that the simulated maximal contractive force appeared at a critical θ of approximately 40°, whereas the measured

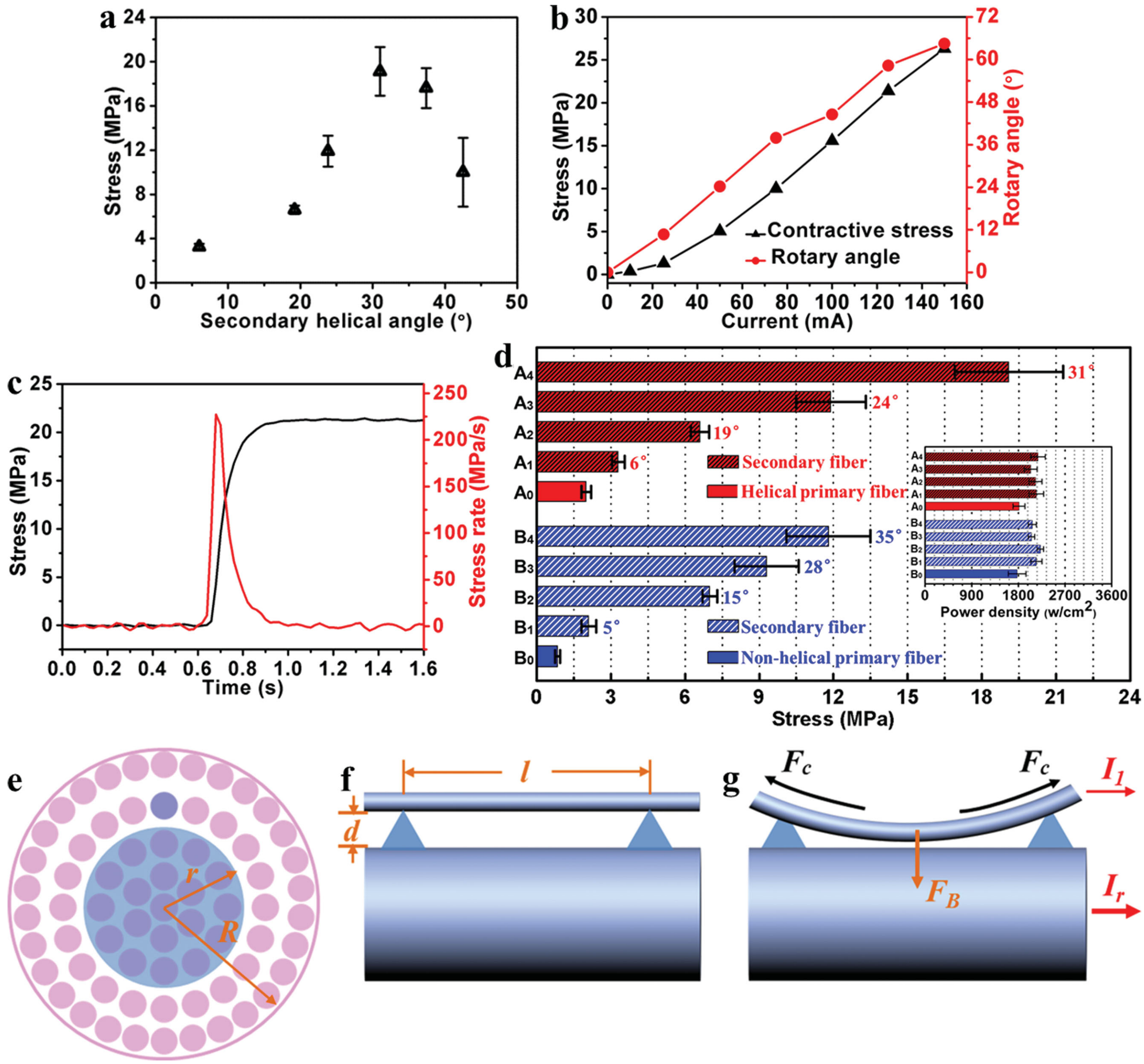

Figure 4. Electromechanical actuations of the secondary fibers. a) Dependence of contractive stress on secondary helical angle upon pass of the same current of 125 mA. b) Dependence of contractive stress and rotary angle on current under the same secondary helical angle of 31°. Here the point at the top one-fifth part was studied as a demonstration. c) Dependence of the contractive stress (black line) and stress rate (red line) on time. d) Contractive stresses of the primary and secondary fibers with increasing helical angles. A_0 and B_0 correspond to the twisted (helical angle of 32°) and non-twisted, respectively, primary fibers upon applying a current of 2.5 mA. A_1, A_2, A_3, and A_4 correspond to secondary fibers assembled from 50 twisted primary fibers (helical angle of 32°) with increasing secondary helical angles of appropriately 6°, 19°, 24°, and 31°, respectively. B_1, B_2, B_3 and B_4 correspond to secondary fibers assembled from 50 non-twisted primary fibers with increasing secondary helical angles of approximately 5°, 15°, 28°, and 35°, respectively. The applied current for A_1-A_4 and B_1-B_4 was the same as the 125 mA current application. The inserted graph shows the cross-sectional power density. e) Cross-sectional view of a fiber. f, g) Side views of the labelled unit and circled area at (d) before and after, respectively, the application of electric current.

critical helical angles appear at 32° and 31° for the primary and secondary fibers, respectively (Figures 4a and S12b). This difference was explained by the following two observations. First, the distances among MWCNTs decreased as the helical angle increased; thus, more and more electrons hopped among the MWCNTs rather than to move along the axis.[24,25] The hopping conduction did not contribute to the attractive force among the MWCNTs; thus, the electromagnetic forces among the MWCNTs were decreased as the helical angle increased. Second, as shown in Figure S18, the moduli at the helical angles of 0°, 8°, and 16° were similar, whereas the modulus was much lower at a higher helical angle, such as 43°. Therefore, the mechanical behaviour was largely changed due to the over-twisting at a higher helical angle with decreasing contractive stress. For the secondary fibers, a similar relationship existed between the modulus and the helical angle (Figure S19).

The above electromechanical actuations and applications were performed in air. We had also investigated other environmental media, such as water and electrolyte solutions, and the electromechanical actuations were observed for these fiber muscles (Movie S9). Here the twisted MWCNT fibers were prepared by a dry-spinning process, and for the twisted MWCNT fibers synthesized by the other methods such as floating catalyst CVD method, the same phenomenon had been also observed. The combined mechanism based on Ampere's Law and the Law of the Lever at the nanoscale level could also be generalised to develop a series of electromechanically torsional materials through the helical and aligned arrangement of conductive one-dimensional nanostructures, such as nanowires and other nanotubes.[26–29]

Experimental Section

Experimental details are included in the Supporting Information.

Supporting Information

Supporting Information is available from the Wiley Online Library or from the author.

Acknowledgements

The authors thank Professor Yuliang Yang for the kind suggestions. This work was supported by MOST (2011CB932503, 2011CB605700), NSFC (21225417, 21104010), STCSM (12nm0503200), the Fok Ying Tong Education Foundation, the Program for Special Appointments of Professors at Shanghai Institutions of Higher Learning, and the Program for Outstanding Young Scholars from the Organization Department of the CPC Central Committee.

Received: June 28, 2014
Revised: August 24, 2014
Published online: December 2, 2014

[1] R. Dudley, *The Biomechanics of Insect Flight: Form, Function, Evolution*, Princeton University Press, Princeton, NJ, USA **2002**.
[2] M. H. Dickinson, C. T. Farley, R. J. Full, M. A. R. Koehl, R. Kram, S. Lehman, *Science* **2000**, *288*, 100.
[3] G. K. Taylor, *Biol. Rev.* **2001**, *76*, 449.
[4] D. Warrick, T. Hedrick, M. J. Fernandez, B. Tobalske, A. Biewener, *Curr. Biol.* **2012**, *22*, R472.
[5] J. D. Madden, *Science* **2007**, *318*, 1094.
[6] D. B. Li, W. F. Paxton, R. H. Baughman, T. J. Huang, J. F. Stoddart, P. S. Weiss, *Mrs Bull.* **2009**, *34*, 671.
[7] K. Y. Ma, P. Chirarattananon, S. B. Fuller, R. J. Wood, *Science* **2013**, *340*, 603.
[8] R. H. Baughman, C. X. Cui, A. A. Zakhidov, Z. Iqbal, J. N. Barisci, G. M. Spinks, G. G. Wallace, A. Mazzoldi, D. De Rossi, A. G. Rinzler, O. Jaschinski, S. Roth, M. Kertesz, *Science* **1999**, *284*, 1340.
[9] W. Guo, C. Liu, F. Zhao, X. Sun, Z. Yang, T. Chen, X. Chen, L. Qiu, X. Hu, H. Peng, *Adv. Mater.* **2012**, *24*, 5379.
[10] M. Schulz, *Science* **2012**, *338*, 893.
[11] S. Iijima, *Nature* **1991**, *354*, 56.
[12] M. M. J. Treacy, T. W. Ebbesen, J. M. Gibson, *Nature* **1996**, *381*, 678.
[13] M. Miao, *Carbon* **2011**, *49*, 3755.
[14] S. Berber, Y. K. Kwon, D. Tomanek, *Phys. Rev. Lett.* **2000**, *84*, 4613.
[15] A. Peigney, C. Laurent, E. Flahaut, R. R. Bacsa, A. Rousset, *Carbon* **2001**, *39*, 507.
[16] M. Zhang, K. R. Atkinson, R. H. Baughman, *Science* **2004**, *306*, 1358.
[17] X. M. Sun, T. Chen, Z. B. Yang, H. S. Peng, *Acc. Chem. Res.* **2013**, *46*, 539.
[18] G. Z. Sun, J. Q. Liu, L. X. Zheng, W. Huang, H. Zhang, *Angew. Chem. Int. Ed.* **2013**, *52*, 13351.
[19] T. Mirfakhrai, J. Madden, R. Baughman, *Mater. Today* **2007**, *10*, 30.
[20] A. M. Wilson, J. C. Lowe, K. Roskilly, P. E. Hudson, K. A. Golabek, J. W. McNutt, *Nature* **2013**, *498*, 185.
[21] Y. K. Kwon, S. Berber, D. Tománek, Phys. Rev. Lett. **2004**, 92.
[22] Y. Maniwa, R. Fujiwara, H. Kira, H. Tou, H. Kataura, S. Suzuki, Y. Achiba, E. Nishibori, M. Takata, M. Sakata, A. Fujiwara, H. Suematsu, *Phys. Rev. B* **2001**, *64*, 241402.
[23] F. Meng, X. Zhang, R. Li, J. Zhao, X. Xuan, X. Wang, J. Zou, Q. Li, *Adv. Mater.* **2014**, *26*, 2480.
[24] H. S. Peng, M. Jain, Q. W. Li, D. E. Peterson, Y. T. Zhu, Q. X. Jia, *J. Am. Chem. Soc.* **2008**, *130*, 1130.
[25] Y. Wei, K. Jiang, X. Feng, P. Liu, L. Liu, S. Fan, *Phys. Rev. B* **2007**, *76*, 045423.
[26] G. Z. Sun, J. Q. Liu, X. Zhang, X. W. Wang, H. Li, Y. Yu, W. Huang, H. Zhang, P. Chen, *Angew. Chem. Int. Ed.* **2014**, *53*, 12576.
[27] S. V. N. T. Kuchibhatla, A. S. Karakoti, D. Bera, S. Seal, *Prog. Mater. Sci.* **2007**, *52*, 699.
[28] Y. N. Xia, P. D. Yang, Y. G. Sun, Y. Y. Wu, B. Mayers, B. Gates, Y. D. Yin, F. Kim, Y. Q. Yan, *Adv. Mater.* **2003**, *15*, 353.
[29] N. P. Dasgupta, J. Sun, C. Liu, S. Brittman, S. C. Andrews, J. Lim, H. Gao, R. Yan, P. Yang, *Adv. Mater.* **2014**, *26*, 2137.